Journal Pre-proofs

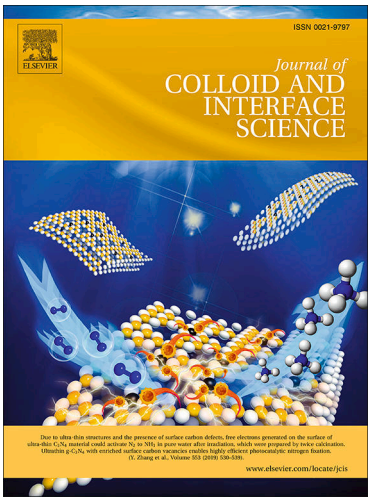

Regular Article

Nitrogen-doped carbon encapsulated zinc vanadate polyhedron engineered from a metal−organic framework as a stable anode for alkali ion batteries

Yixing Fang, Yilan Chen, Lingxing Zeng, Tao Yang, Qinxin Xu, Yiyi Wang, Shihan Zeng, Qingrong Qian, Mingdeng Wei, Qinghua Chen

PII: S0021-9797(21)00260-5
DOI: https://doi.org/10.1016/j.jcis.2021.02.108
Reference: YJCIS 27652

To appear in: *Journal of Colloid and Interface Science*

Received Date: 23 November 2020
Revised Date: 23 February 2021
Accepted Date: 24 February 2021

Please cite this article as: Y. Fang, Y. Chen, L. Zeng, T. Yang, Q. Xu, Y. Wang, S. Zeng, Q. Qian, M. Wei, Q. Chen, Nitrogen-doped carbon encapsulated zinc vanadate polyhedron engineered from a metal−organic framework as a stable anode for alkali ion batteries, *Journal of Colloid and Interface Science* (2021), doi: https://doi.org/10.1016/j.jcis.2021.02.108

Nitrogen-doped carbon encapsulated zinc vanadate polyhedron engineered from a metal−organic framework as a stable anode for alkali ion batteries

Yixing Fang[a,‡], Yilan Chen[a,‡], Lingxing Zeng[*a, c, e], Tao Yang[d], Qinxin Xu[a], Yiyi Wang[a], Shihan Zeng[a], Qingrong Qian[a, c, e], Mingdeng Wei[b], and Qinghua Chen[*a, c]

[a] Engineering Research Center of Polymer Green Recycling of Ministry of Education, College of Environmental Science and Engineering, Fujian Normal University, Fuzhou, Fujian 350007, China.

[b] Fujian Provincial Key Laboratory of Electrochemical Energy Storage Materials, Fuzhou University, Fuzhou, Fujian 350002, China.

[c] Fujian Key Laboratory of Pollution Control & Resource Reuse, Fuzhou, Fujian 350007, China.

[d] TEMA-NRG, Mechanical Engineering Department University of Aveiro, 3810-193 Aveiro, Portugal.

[e] Key Laboratory of Advanced Energy Materials Chemistry (Ministry of Education), College of Chemistry, Nankai University, Tianjin 300071, China.

[*] Corresponding authors. Tel. & Fax: +86-591 8346 5158
zenglingxing@fjnu.edu.cn (L. Zeng), cqhuar@126.com (Q. Chen)
‡ These authors contributed equally to this work.

ABSTRACT

In this work, we fabricated vanadium/zinc metal−organic frameworks (V/Zn-MOFs) derived from self-assembled metal organic frameworks, to further disperse ultrasmall Zn_2VO_4 nanoparticles and encapsulate them in a nitrogen-doped nanocarbon network (ZVO/NC) under *in situ* pyrolysis. When employed as an anode for lithium-ion batteries, ZVO/NC delivers a high reversible capacity (807 mAh g^{-1} at 0.5 A g^{-1}) and excellent rate performance (372 mAh g^{-1} at 8.0 A g^{-1}). Meanwhile, when used in sodium-ion batteries, it exhibits long-term cycling stability (7000 cycles with 145 mAh g^{-1} at 2.0 A g^{-1}). Additionally, when employed in potassium-ion batteries, it also shows outstanding electrochemical performance with reversible capacities of 264 mAh g^{-1} at 0.1 A g^{-1} and 140 mAh g^{-1} at 0.5 A g^{-1} for 1000 cycles. The mechanism by which the pseudocapacitive behaviour of ZVO/NC enhances battery performance under a suitable electrolyte was probed, which offers useful enlightenment for the potential development of anodes of alkali-ion batteries. The performance of Zn_2VO_4 as an anode for SIBs/PIBs was investigated for the first time. This work provides a new horizon in the design ZVO/NC as a promising anode material owing to the intrinsically synergic effects of mixed metal species and the multiple valence states of V.

KEYWORDS: Zn_2VO_4; Metal-organic framework; N-doped carbon; Anode; Alkali ion batteries

1. Introduction

As a kind of clean and efficient renewable-energy storage device, rechargeable batteries have been regarded as an indispensable electrochemical system. Commercialized lithium-ion battery (LIB) technology is the dominant power supply for portable electronics and electric vehicles [1]. However, limited lithium resources and t exorbitant prices have made it difficult to meet the demands of excessive growth in emerging markets, particularly, large-scale stationary power stations [2]. Hence, sodium-ion batteries (SIBs) and potassium-ion batteries (PIBs) have aroused great interest as alternatives to lithium-ion batteries [3]. More importantly, the redox potentials of sodium (−2.71 V) and potassium (−2.93 V) are lower than that of lithium (−3.04 V) [4, 5]. Lithium-ion batteries (LIBs) are limited by the lack of suitable anode materials, such as graphite (35 mAh g^{-1} for SIBs/279 mAh g^{-1} for PIBs) [6-8], which restricts the development of energy storage equipment. Because of the significantly larger radius of alkali ions (Li^+< Na^+< K^+, 0.76< 1.0 < 1.38 Å), developing and designing comparable novel anode materials for alkali ion batteries remains a rigorous challenge.

In addition to graphite, studies investigated non-carbonaceous materials as anodes, including transition metal oxides (TMOs), transition metal chalcogenides (TMCs), and intermetallic and organic compounds [9-11]. Among them, transition bimetallic oxides, possess high capacities benefiting from multiple redox reactions, as well as the interfacial and synergistic effects of multiple metal species, such as $MnFe_2O_4$, $NiCo_2O_4$, $FeCo_2O_4$, and $CuCo_2O_4$ [12-15]. These TMOs generally suffer from large volume

changes during the charge/discharge process, resulting in capacity fading and shorter lifetimes. Additionally, the ionic radius of K^+ is larger than that of Li^+ and Na^+, and the dynamics of K^+ are kinetically more sluggish as compared to Li^+/Na^+ [16-18].

To overcome these issues, bimetallic vanadates have been widely considered as candidate for anodes, including Co_2VO_4, $Ni_3V_2O_8$, ZnV_2O_4, $FeVO_4$, and CaV_4O_9 [19-24]. For instance, novel nanosheet-assembled compact CaV_4O_9 microflowers were designed by Mai et al., which show great areal capacity and long-cycling performance with superior mass loadings for LIBs and SIBs [21]. Guo's group reported amorphous $FeVO_4$ as an anode material for PIBs with superior capacity (~350 mAh g^{-1}) [22]. In particular, zinc vanadate ($Zn_xV_yO_z$) compounds have attracted the attention of researchers for energy storage systems owing to their lower cost, better availability, environmental friendliness, and broad diversity of species and architectures (ZnV_2O_4 glomerulus nano/microspheres, porous sheet-like $Zn_3V_2O_8$, grass-like $Zn_3V_3O_8$ nanobelts and so on) [25-28]. In our previous works, ZnV_2O_4–CMK nanocomposites and hierarchical lychee-like $Zn_3V_3O_8$@C/rGO nanospheres were investigated as anode materials for LIBs, demonstrating excellent electrochemical properties [29, 30]. Additionally, zinc vanadate infused electrochemical activities are due to the variable architecture and valence states of vanadium for the insertion/disinsertion of sodium-ions [31-34]. For example, Liu's group synthesized the m-ZnV_2O_6 nanobelt which exhibits an excellent discharge capacity of 247 mAh g^{-1} at the 100th cycle for SIBs [31]. Regarding PIBs, to date, little work on bimetallic vanadates, especially zinc vanadates, has been reported.

The Zn-based zeolitic imidazolate framework (ZIF-8), which consists of zinc ions (centre) and 2-methylimidazole (an organic ligand), has been developed as a type of organic–inorganic hybrid nanoporous crystal material, forming a three-dimensional polyhedral structure and showing great enhancement in the field of energy storage systems [35-39]. In contrast to bimetallic vanadates previously reported in different architectural designs, typical carbon nanocomposites were was obtained by hydrothermal or solvent-thermal reduction strategies. Nevertheless, it is generally difficult to design and synthesize carbon-encapsulated bimetallic vanadate nanostructures by the solid-state method. Considering the high porosity of ZIF-8 with sodalite (SOD)-type cavities of 12.5 Å effective diameter, it is feasible to synthesize bimetallic vanadate by one-step solid-state calcination, placing V species into these suitable cavities [40, 41].

Herein, we ingeniously designed a Zn-MOF *in situ* derived carbon matrix to introduce vanadium species. Nitrogen-doped carbon encapsulated ultrasmall Zn_2VO_4 nanoparticles were synthesized and dispersed homogenously within the carbon cavity, as illustrated in Scheme 1. Enclosed polyvinyl pyrrolidone (PVP) not only acts as a surface capping agent [42, 43], but can also be derived as a carbon-based protective layer, restricting the direct contact of Zn_2VO_4 nanoparticles with the electrolyte and providing an additional pseudocapacitive effect. In view of the physical barrier and heterogeneous-phase confinement, the ultrasmall zinc vanadate crystals with pure phases are well confined within the nanoporous carbon network. The synthesized N-doped carbon encapsulated Zn_2VO_4 polyhedron (ZVO/NC) presents high specific

capacity, stable long-term cycling performance and improved rate performance with enhanced electrical conductivity. Both the rational design structure and superior electrochemical performance demonstrate that ZVO/NC is a desirable candidate for an anode for alkali ion batteries.

2. Experimental Section

All reagents were used without further purification. Polyvinyl pyrrolidone (PVP, Mw =40000) was purchased from Sigma-Aldrich (St. Louis, MO, USA). Vanadyl acetylacetonate ($VO(acac)_2$, 99%) was purchased from Aladdin (Shanghai, China). $Zn(NO_3)_2 \cdot 6H_2O$, N, N-dimethylformamide (DMF, AR) and 2-Methylimidazole (AR) were purchased from Sinopharm Chemical Reagent Co., Ltd (Shanghai, China).

2.1 Synthesis of the V/Zn-MOF precursor.

The precursor (V/Zn-MOF) was synthesized with a modified version of the literature procedures [44]. $Zn(NO_3)_2 \cdot 6H_2O$ (1.0 mmol, 0.2975 g), 0.5 mmol of vanadyl acetylacetonate and 0.2 g of PVP (MW = 40000) were dissolved in a solvent mixture containing 20 mL of deionized water (DI) and 20 mL of DMF by stirring for 30 mins at room temperature to form solution A. Then, 4.0 mmol of 2-methylimidazole was dissolved in a mixed solvent of 20 mL of DI and 20 mL of DMF by stirring for 30 mins to form solution B. Then, solution B was slowly poured into solution A and stirred constantly and rapidly until well mixed. After 30 mins of vigorous stirring the reaction mixture was left to age for 20 h. Finally, the pine green precipitate was washed with DMF and DI several times, and dried at 70 °C.

2.2 Synthesis of ZVO/NC and ZVO/ZO/NC.

ZVO/NC was fabricated by a one-step calcination of the as-prepared precursor in a furnace and calcined at 700 °C for 4 h in Ar flow with a heating rate of 2 °C min^{-1}. For comparison, the contrast sample was prepared using a similar approach with annealing at 500 °C (denoted as ZVO/ZO/NC).

2.3 Structural characterization.

The crystal phases of the samples were analysed in an X-ray diffractometer (XRD, Bruker D8 diffractometer, Germany) with Cu-Kα radiation (λ=0.15406 nm) in the range of 5-80°. The morphologies of the products were determined by scanning electron microscopy (SEM, Hitachi 4800) and transmission electron microscopy (TEM, FEI F20 S-TWIN). Energy dispersive X-ray spectrometry (EDS) was performed using TEM. X-ray photoelectron spectroscopy (XPS, ESCALAB MARK II spherical analyser) was used to estimate the elemental valence. The specific surface area and pore size distribution were recorded using the Brunauer-Emmett-Teller (BET) method. Raman spectroscopy (DXR2xi) was also employed. The sample's thermal properties were evaluated by thermogravimetric analysis (TGA; TA-SDT Q600 analyser). TGA was measured from the ambient temperature to 800 °C in an air atmosphere at a heating rate of 10 °C min^{-1}.

2.4 Electrochemical Measurements.

For the LIB test, the working electrode was obtained by mixing the ZVO/NC or ZVO/ZO/NC samples, super-P and polyvinylidene fluoride (PVDF) in N-methyl-2-pyrrolidone at a weight ratio of 8 : 1 : 1. The solvents eventually evaporated, and the

electrode films were dried at 110 °C under vacuum for 10 h. A 1 M solution of $LiPF_6$ in ethylene carbonate (EC)/dimethyl carbonate (DMC)/ethyl methyl carbonate (EMC) (1:1:1 by volume) served as the electrolyte. Lithium metal foil was used as the reference electrode, and Celgard 2320 was used as the separator. For SIB and PIB tests, the working electrodes were prepared following the same procedure with a mass ratio of the ZVO/NC or ZVO/ZO/NC samples, super-P, and carboxymethyl cellulose (CMC) of 8: 1: 1. Sodium or potassium metal foil was used as the reference electrode, and Whatman glass fibre was used as the separator. $NaPF_6$ (1 M) including ethylene carbonate (EC)/dimethyl carbonate (DMC)/ethyl methyl carbonate (EMC) (1:1:1 by volume) was used as the electrolyte for SIBs. KPF_6 (1 M) was dissolved in ethylene carbonate (EC)/diethyl carbonate (DEC) (1:1 by volume) as the electrolyte for PIBs. The mass loading on each electrode for LIBs, SIBs and PIBs can be calculated with the value of 1.0-1.5 mg, respectively. The galvanostatic charge-discharge curves and charge-discharge performance were tested with Land CT 2001A battery instruments. The cyclic voltammograms (CV; Ivium, Netherlands) were collected on an electrochemical workstation at room temperature in the voltage range 0.01 - 3.0 V. Electrochemical impedance spectroscopy (EIS) was carried out at frequency range of 10^{-1} Hz to 10^5 Hz with a voltage disturbance amplitude 1.0 mV.

3. Results and discussion

3.1. Structure and morphology characterization

Powder XRD measurements were utilized to characterize the patterns of all samples (**Figure 1a**). The XRD pattern of V/Zn-MOF (the precursor) is shown in **Figure S1a**.

The precursor exhibits distinct crystals with cubic *I*43 m groups and strong diffraction peaks (labelled as "♥") at 2θ values of 7.4, 10.4, 12.8, 14.7, 16.5, and 18.1°, which match the (011), (002), (112), (022), (013) and (222) crystals of well-known ZIF-8 structures, respectively [45]. When elevating the calcination temperature to 500 °C, the precursor (V/Zn-MOF) was converted *in situ* into a ZVO/ZO/NC composite. That the distinguishable peaks (labelled as "♦") located at 31.7, 34.3, and 36.2° are ascribed to the (100), (002), and (101) planes of ZnO (JCPDS No.80-0074), respectively [46]. Then, with increasing calcination temperature, single phase, well-crystallized Zn_2VO_4 was obtained at 700 °C. The pattern of ZVO/NC is the same as that of ZVO/ZO/NC and no impurity peaks (ZnO) appear in the red pattern. The diffraction peaks of ZVO/NC become sharper, demonstrating the growth of crystallites and enhanced crystallinity. The strong diffraction peaks are located at 18.3, 30.1, 35.4, 37.1, 43.1, 53.4, 56.9 and 62.5°, which correspond well to the (111), (220), (311), (400), (422) (511) and (440) crystal planes of standard cubic Zn_2VO_4 (JCPDS No. 76-1632) [47]. A continuous increase in annealing temperature leads to the *in situ* formation of the Zn_2VO_4 polyhedron composite with a strongly coupled carbon matrix. The broad yet distinguishable peaks of ZVO/ZO/NC and ZVO/NC at approximately 26° indicate that the carbon matrixes derived from ZIF-8 are amorphous carbon structures. **Figure 1b** shows the Raman spectra of the ZVO/ZO/NC and ZVO/NC composites. Broad D-band (disordered band) and G-band (graphite band) peaks are seen ca. 1360 and 1599 cm^{-1}. As the calcination temperature increases, the calculated value of the peak intensity ratio for ZVO/NC (I_D/I_G = 1.12) becomes larger than that of ZVO/ZO/NC (I_D/I_G = 1.08),

revealing the increase in carbon defects in the ZVO/NC structure. Abundant carbon defects, possibly introduced by N heteroatom doping, are beneficial for enhancing extra alkali ion storage sites [48]. Thermogravimetric analysis (TGA) was conducted to further characterize the carbon content within ZVO/NC in air (**Figure 1c**). The weight loss of ZVO/NC (ca. 15 wt. %) below 200 °C is because of the evaporation of adsorbed moisture. Based on a consecutive weight loss of carbon between ca. 200 and 700 °C, the carbon and Zn_2VO_4 contents of ZVO/NC can be calculated to be ca. 55 wt. % and 45 wt. %, respectively. The BET surface area and pore volume of V/Zn-MOF are calculated to be 1062 $m^2\ g^{-1}$ and 0.184 $cm^3\ g^{-1}$, respectively **(Figure S1d**). Through a Barrett-Joyner-Halendar (BJH) evaluation, the pore-size distribution is indicative of average mesopores of 2.2 nm within V/Zn-MOF, as shown in **Figure S1d** (inset). The specific surface area of the ZVO/NC is 351 $m^2\ g^{-1}$ with diameters centred at 3.2 nm (**Figures 1d and inset**). The larger specific surface area of the ZVO/NC polyhedron and abundant pore networks can shorten the ion transport distance and enhance the electrode/electrolyte contact area.

The elemental composition of the ZVO/NC polyhedron was further confirmed by XPS (**Figure 2**). The XPS spectra on the ZVO/NC surface reveal the characteristic signals of Zn, V, O, C and N without impurities (**Figure 2a**). In the Zn 2p XPS spectrum (**Figure 2c**), two obvious peaks are detected at 1021.7 and 1044.8 eV, corresponding well to Zn $2p_{3/2}$ and Zn $2p_{1/2}$ spin orbitals, respectively, confirming the Zn^{2+} state of Zn. For the high-resolution V 2p spectra, there are three peaks of V^{3+}, V^{4+}, and V^{5+} at 515.9, 517.1, and 517.4 eV, respectively. The primary peak was located at a binding energy

of 517.1 eV, implying the presence of V^{4+} (highlighted by a light blue colour) in Zn_2VO_4 [49-51]. Likewise, as shown in **Figure 2d**, four peaks of the O 1s spectrum are located at approximately 529.8, 530.5, 531.7 and 532.9 eV, which correspond to lattice oxygen, Zn-O and V-O, C=O (carbonate), and C-O-C (carbonate) species, respectively [52]. In addition, defects and dopants are two important factors influencing the electrochemical performance [53]. As shown in **Figure 2e**, the peaks at approximately 284.8, 285.3, 286.9 and 289.5 eV are associated with C=C, C=N, C-O and C=O bonds, respectively. This validates the successful *in situ* N atom doping in the carbon matrix, which is consistent with the above results of Raman spectrum. The N 1s spectrum (**Figure 2f**) are deconvolved into three types of nitrogen species located at 398.6, 400.2 and 401.2 eV, which can be interpreted as the pyridinic N, pyrrolic N, and graphitic N, respectively. In detail, the presence of pyridinic N and pyrrolic N is believed to induce many highly chemically active sites at the edges or in the defect sites of the basal plane while graphitic N can enhance the conductivity and stability of nanocomposites [54-56]. As shown in **Figure 2g**, the relative ratios of pyridinic N, pyrrolic N, and graphitic N are 49.4, 30.1, and 20.5%, respectively. Additionally, according to the results of elemental analysis (**Table S1**), the carbon and nitrogen contents in ZVO/NC ca. 35.13 and 10.65 wt%, respectively. N-doped activated carbon has been taken into account for the active sites for the electrochemical reaction process, which can not only improve the surface wettability between organic electrolytes and active materials, but also facilitate the adsorption and charge-transfer ability of Li/Na/K ions, accelerating the pseudo-capacitance behaviour.

The architecture of ZVO/NC was analysed by SEM and TEM characterizations (**Figure 3**). As depicted in **Figure S2a**, V/Zn-MOF was initially prepared as a precursor to fabricate ZVO/NC. The precursors are monodispersed with sizes ranging between 200 and 400 nm and possess regular polyhedron morphology. The V/Zn-MOF precursor was transformed into ZVO/ZO/NC via calcination at 500 °C (**Figure S2b**). The structure of the polyhedron is well maintained while the surface becomes rough after increasing the calcination temperature to 700 °C (**Figure 3a-b**). However, the structure of the polyhedron undergoes visible damage after increasing the calcination temperature to 800 °C under an Ar atmosphere (**Figure S2d**), suggesting the importance of proper calcination temperature to the structure of the polyhedron. As shown in **Figure 3c**, owing to the strong interaction between carbon layers derived from PVP and the rhomboid dodecahedron carbon skeleton derived from V/Zn-MOF, the overgrowth of Zn_2VO_4 nanoparticles is restricted in the carbon matrix, leading to the formation of a sweetsop-like shell configuration. The dodecahedral configuration of ZVO/NC can be well preserved from V/Zn-MOF with a higher calcination temperature and the entire structures have a uniform size distribution of approximately 100-300 nm, quite similar to that of V/Zn-MOF. TEM images show further insight into the interior architecture of the ZVO/NC polyhedron. The low-magnification TEM images (**Figure 3d-e**) provide evidence of the scale-uniformity of the dodecahedra with similar thicknesses. Furthermore, **Figure 3e** reveals numerous Zn_2VO_4 nanoparticles with high crystallinity that are tightly and homogeneously confined within the carbon matrix. Lattice fringes of 0.242, 0.209 and 0.171 nm are well indexed to the (222), (400) and

(422) lattice planes of Zn_2VO_4, respectively. The corresponding EDS mappings in **Figure 3f** reveal the homogeneous distribution of Zn, V, O, C, and N, which demonstrates that all atoms are uniformly dispersed into the N-doped carbon matrix.

3.2. Electrochemical properties

3.2.1. Electrochemical performance for LIBs

The electrochemical performances of ZVO/NC as the anode material of LIBs is shown in **Figure 4**. In the CV curves for ZVO/NC at a scan rate of 0.1 m V s^{-1} (**Figure 4a**), two broad reduction peaks ca. 1.46 V and 0.55 V appeared, which correspond to the first lithium intercalation of Zn_2VO_4 to form Li_xVO_2 and the conversation reaction to form ZnO in the initial cathodic cycle[57]. Moreover, a third sharp intense peak is found below 0.1 V and has asymmetrical features. This peak of the first reduction curve is larger than other curves below approximately 0.1 V which are attributed to the consumption of part of the electrolyte, forming a solid electrolyte interphase (SEI) film[58]. The intense asymmetric peak below 0.1 V arises from the overlapping of two peaks related to an irreversible Li^+ conversion reaction that results in the formation of Li-Zn alloy due to the further reduction of ZnO into Zn. In contrast, the initial anodic sweep displays three oxidation peaks: one weak peak at approximately 0.53 V (below 1.0 V) corresponds to delithiation process of the Li-Zn alloy[47]. The other two peaks at 1.22 and 2.62 V should be ascribed to oxidization of Zn to ZnO and extraction of Li ions from Li_xVO_2 matrices, accompanied by transformations of V^{2+} to V^{3+}, and V^{3+} to V^{4+}, respectively [59]. The lithiation and conversion reaction of Zn_2VO_4 for LIBs may be expressed as follows [60, 61]:

$$Zn_2VO_4 + xLi^+ + xe^- \rightarrow 2ZnO + Li_xVO_2 \quad (1)$$

$$ZnO + 2Li^+ + 2e^- \leftrightarrow Zn + Li_2O \quad (2)$$

$$Zn + yLi^+ + ye^- \rightarrow Li_yZn \quad (3)$$

Figure 4b displays that the initial discharge and charge capacities of the ZVO/NC electrode are 1111 and 619 mAh g^{-1} at 0.5 A g^{-1}, respectively. The irreversible capacity loss at the 1st cycle can be ascribed to the formation of an SEI layer, which is consistent with the CV curve results. Additionally, the discharge capacities for the 2nd, 3rd, 50th, 100th and 200th cycles of ZVO/NC are 675, 662, 666, 786 and 807 mAh g^{-1}, respectively, indicating the good reversibility and capacitance stability of ZVO/NC. **Figure 4c** shows the cycling performances of the ZVO/NC and ZVO/ZO/NC electrodes at 0.5 A g^{-1} for 200 cycles. ZVO/NC presents the an excellent initial capacity (1111 mAh g^{-1}) and maintains stable capacity of 619 mAh g^{-1} after 200 cycles. ZVO/NC delivers the best high-rate performance and benign capacity retention at large current densities as shown in **Figure 4d**. The average reversible capacities of the ZVO/NC electrode are 658, 604, 532, 442, 397 and 372 mAh g^{-1}, at current densities of 0.5, 1.0, 2.0, 4.0, 6.0 and 8.0 A g^{-1}, respectively. The ZVO/NC electrode even maintains a discharge capacity of 718 mAh g^{-1} when the rate returns to 0.5 A g^{-1}. The cycling capability of the ZVO/NC electrode (441 mAh g^{-1}) was further evaluated at an ultrahigh rate of 5.0 A g^{-1} with a long lifespan of 1000 cycles, as shown in **Figure 4e**. The Coulombic efficiency of the ZVO/NC anode approaches to 100% with a capacity retention approximately 83.2% just after several cycles.

To further investigate the reason for the enhanced cycling stability and rate capability of ZVO/NC electrodes, CV curves from 0.2 to 10.0 mV·s^{-1} were produced (**Figure 5a**). Specifically, the relationship of the measured peak current (i) and scan rate (v) can be described by the following two equations [62, 63]:

$$i = a \cdot v^b \quad (4)$$

$$\log i = b \cdot \log v + \log a \quad (5)$$

where both a and b are controllable constant parameters. The value of factor b ranged from 0.5 (diffusion-controlled process) to 1.0 (capacitive process). In this case, the relationship between log i and log v of the ZVO/NC electrodes (**Figure 5b**), the calculated b values are 0.84 ± 0.012 (peak-A) and 0.81 ± 0.013 (peak-B), respectively, which means that Li^+ storage is influenced by both diffusion-controlled and pseudocapacitance processes. The capacitive contribution can be calculated from the following equation [64]:

$$i_{(v)} = k_1 v + k_2 \cdot v^{1/2} \quad (6)$$

where $i_{(v)}$, v, k_1 and k_2 are the measured current, fixed potential V, scan rate, and adjustable constant parameters, respectively. As illustrated in **Figure 5c**, the pseudocapacitive contribution reaches 43% at 1.0 mV s^{-1}. The capacitive contributions of the ZVO/NC electrodes gradually increase as the scan rate v shifts (from 0.2 to 10 mV s^{-1}), as shown in **Figure 5d**. These results demonstrate that the existence of pseudocapacitive behaviour can effectively improve electrochemical performance, resulting in kinetics which facilitate storage of Li ions on the surface or in the near

surface region, as well as creating superior long cycling performance and rate capability.

3.2.2. Electrochemical performance for SIBs

Considering the promising behaviour of the as the ZVO/NC anode for lithium storage, we further studied its capability in sodium ion batteries. To optimize the performance of the ZVO/NC electrode for SIBs, different electrolytes (ester-based or ether-based) were given priority for investigation [65]. Several factors deserve attention, such as the various Na-salts ($NaPF_6$, $NaClO_4$ or $NaCF_3SO_3$) and solvents including propylene carbonate (PC), ethylene carbonate (EC), diethyl carbonate (DEC), dimethyl carbonate (DMC), ethyl methyl carbonate (EMC), dimethoxyethane (DME) and diethylene glycol dimethyl ether (DIGLYME) or mixtures thereof. To illustrate the significance of the electrolytes and corresponding solvents, the electrochemical behaviours of the ZVO/NC electrode using different electrolytes were also examined. As shown in **Figure 6a**, when using 1.0 M $NaPF_6$ in EC/DMC/EMC as the electrolyte, the ZVO/NC electrode exhibits the highest reversible capacity performance. As a contrast, when using 1.0 M $NaClO_4$ in EC/DMC/EMC or 1.0 M $NaPF_6$ in PC, the ZVO/NC electrode displays a lower capacity (ca. 170 mAh g^{-1}) at 0.1 A g^{-1}. On the other hand, compared with ester-type solvents (EC/DMC/EMC and PC), when using ether-type solvents including DME or DIGLYME, the ZVO/NC electrode suffers a sharp capacity decay to less than 150 mAh g^{-1} or even less after 50 cycles. Consequently, the results have demonstrated that the cycling performance of ZVO/NC in ester-based electrolytes is

superior to that in ether-based systems. This ternary mixture may be able to provide efficient ionic conductivity, low viscosity, low ion pairing, and, more significantly, the formation of opportune and stable SEI films. As shown in **Figure S3a**, CV curves of ZVO/NC at 0.1 mV s^{-1} were obtained in the voltage range between 0.01 and 3.00 V (versus Na^+/Na). For the initial cathodic cycle, the reduction peak of approximately 1.0 V is different from the subsequent scans likely due to the formation of the solid electrolyte SEI membrane. One broad anodic peak centre at 1.0-1.25 V is assigned to the oxidation reaction. From the 2nd cycle onward, the CV curves substantially overlap, representing superior reversible Na^+ insertion/extraction in ZVO/NC. The corresponding electrochemical performances are displayed in **Figure S3b**. ZVO/NC delivers a stable reversible capacity of 266 mAh g^{-1} after the 100^{th} cycle at 0.1 A g^{-1} in **Figure 6b**. The ZVO/ZO/NC electrode exhibits an inferior capacity of 204 mAh g^{-1} at the 100^{th} cycle. Meanwhile, ZVO/NC displays fascinating reversible charge capacities of 368, 290, 255, 221, 177, 164 and 110 mAh g^{-1} at 0.05, 0.1, 0.2, 0.5, 1.0, 2.0 and 4.0 A g^{-1}, respectively, which were much better than those of ZVO/ZO/NC (**Figure S3c-d**). As displayed in **Figure 6c**, after enduring 1000 cycles at 1.0 A g^{-1}, the maintained capacity and the Coulombic efficiency for ZVO/NC are 185 mAh g^{-1} and close to 99%, respectively. It is especially notable that ZVO/NC demonstrates excellent ultralong cycling stability, delivering a capacity of 145 mAh g^{-1} at 2.0 A g^{-1} after the 7000^{th} cycle, with a coulombic efficiency of almost 100% (**Figure 6d**).

CV measurements of the ZVO/NC anode for SIBs were carried out at a series of scan rates from 0.2 mV s^{-1} to 1.0 mV s^{-1}. As shown in **Figure 7a**, as the scan rates increase,

all the CV curves display similar shapes with a slight potential polarization, implying regular variation of different charge transfer kinetics. **Figure 7b** shows that the *b* values of the ZVO/NC anode are 0.89 ± 0.004 for the anodic peaks and 0.94 ± 0.019 for the cathodic peaks, suggesting that the sodium storage kinetics of the ZVO/NC anode are also a mixture of pseudocapacitive behaviour and ion diffusion control. The detailed pseudocapacitive fraction of the ZVO/NC anode at 0.4 mV s^{-1} is also illustrated in **Figure 7c**. As shown in **Figure 7d**, the pseudocapacitive contribution increases from 76% to 93% as the scan rate increases from 0.2 mV s^{-1} to 1.0 mV s^{-1}. These results verify that the pseudocapacitive behaviour plays a key role in the entire capacity of the ZVO/NC anode. This might be attributed to the effect on the N atom doping in carbon, as there are more redox reactions on the surface of the carbon matrix.

3.2.3. Electrochemical performance for PIBs

In view of the remarkable performance of ZVO/NC in SIBs, PIBs were also assembled and tested. Recently, different electrolytes and organic solvents have been studied as for anode materials for PIBs, which is significant for enhancing the electrochemical performance of K-ion storage. In the literature, the most common electrolyte for PIBs is potassium hexafluorophosphate (KPF_6), which is dissolved in different organic solvents, similar to SIBs. As shown in **Figure 8a**, we can observe that the capacity of the ZVO/NC anode in the EC/DEC electrolyte is higher than those when other organic solvents are used. Utilizing 1.0 M KPF_6 in EC/DEC as the electrolyte, a stable SEI layer forms that can effectively protect against solvent penetration of the

active materials to maintain stablity between the electrode and electrolyte interface, thereby achieving superior electrochemical performances for PIBs [66, 67]. In **Figure 8b**, the ZVO/NC electrode exhibits a superior discharge capacity of 264 mAh g^{-1}, while the capacity of ZVO/ZO/NC is only 159 mAh g^{-1} after the 80th cycle at 0.1 A g^{-1}. The ZVO/NC electrode offers reversible capacities of 280, 242, 198, 169, 139 and 110 mAh g^{-1} at 0.1 to 4.0 A g^{-1}, respectively. Even when the current density returns to 0.1 A g^{-1}, it still exhibits a capacity of 266 mAh g^{-1}. Moreover, even at higher rate current of 0.5 A g^{-1}, a discharge capacity of 140 mAh g^{-1} remain at the 1000th cycle with a Coulombic efficiency of almost 100% (**Figure 8c**). The CV of the ZVO/NC electrode recorded at 0.1 mV s^{-1} within the voltage range of 0.01-3.0 V (versus K/K^+), is shown in **Figure S4a**. There are no obvious redox pair peaks and just one well-defined peak centred *ca.* 0.95 V in the initial cathodic scan, which can be attributed to the formation of nonstoichiometric K^+-intercalated compounds, accompanied by the formation of a stable SEI layer on the electrode/electrolyte interface. After the subsequent anodic scan, the anodic peak is located at 1.37 V which may be due to the reversible extraction of K ions in the electrode. To further ascertain the potassium-ion insertion/extraction reaction kinetics of the ZVO/NC electrode, additional CV measurements were further carried out ranging from 0.2 to 1.0 mV s^{-1}, as shown in **Figure 8d**. The b values could be individually quantified as 0.78 ± 0.011 (cathodic peak) and 0.83 ± 0.010 (anodic peak), which indicates that the reaction dynamics of K^+ are mainly dominated by a surface induced pseudocapacitance behaviour, Such behaviour suggests rapid ionic migration during the K^+ insertion/extraction process, as shown in **Figure 8e**. **Figure 8f**

shows that the ratio of capacitive behaviour is approximately 67% for the specific voltage curve at 0.6 mV s^{-1}, in which the pink shaded domain represents the dominant capacitive contribution in the whole region. **Figure 8g** depicts the histograms of the two processes at diverse scan rates. Distinctly, as the sweep rate of v augments, the capacitive contribution of the ZVO/NC electrode gradually enlarges from 52% to 63%, then 67%, then 73% and finally to 77%. Such a high capacitive contribution can presumably be attributed to the synergistic effect of the uniformly distributed Zn_2VO_4 nanoparticles and superior conductivity of the carbon matrix.

In addition, to comprehensively understand the enhanced electrochemical behaviour of ZVO/NC, we employed electrochemical impedance spectroscopy (EIS) to characterize the electrodes before and after the 5th cycle. The Nyquist plots (**Figure 9**) consist of three parts: the intercept is located at the *x*-axis, the depressed semicircle appears at the high-medium frequency and a slope line presents at low frequency, corresponding to the internal resistance (Rs), the impedance of the SEI layer(R_f) and the charge-transfer impedance of the electrode/electrolyte interface (Rct), and the semi-infinite diffusion of ions [68-72]. According to the equivalent circuit, the special value of each impedance is listed in **Table S2**. The R_f values of the fresh cells were 39.7, 127.7, and 230.5 Ω in LIBs, SIBs and PIBs, respectively. The R_f increased to 46.1, 159.3, and 373.8 Ω after 5 cycles. The comparison of ZVO/NC to other vanadates **(Table S3)** and traditional materials **(Table S4)** for storage performance in the field of alkali ion batteries as reported in previous literature is provided. Despite direct statistical comparisons, zinc vanadate materials are suitable as anodes for LIBs/SIBs

and exhibit decent electrochemical performance. As an anode material for sodium ion batteries, such materials are rarely able to exhibit excellent stability in long cycles (>5000 cycles). Of particular note is the superior electrochemical storage performance of ZVO/NC including the superior reversible capacity (807 mAh g^{-1} after 200 cycles at 0.5 A g^{-1}) for LIBs, the ultralong cycling performance (145 mAh g^{-1} after 7000 cycles at 2.0 A g^{-1}) for SIBs, and the excellent cycle stability (140 mAh g^{-1} after 1000 cycles at 0.5 A g^{-1}) for PIBs. This performance is superior to some representative vanadate anode materials, which should be ascribed to the meticulously tailored polyhedron with an N-doped porous matrix and accessible active sites of ZVO/NC, favour improved electrode/electrolyte interfacial exchange of alkali ions and speedy electron trafficking. This shows that ZVO/NC shows electrochemical performance comparable to those of previous reports.

As demonstrated in **Scheme 2**, the outstanding $Li^+/Na^+/K^+$ storage performance of ZVO/NC can be ascribed to the following characteristics: (i) Each individual polyhedron structure (100-300 nm) behaves as a stable nanoreactor and isolation chamber forming an effective physical barrier and providing heterogeneous-phase confinement for dispersed Zn_2VO_4 nanoparticles. This helps to avoid excessive agglomeration of nanoparticles and ensures better ionic transport kinetics. (ii) The porous characteristics and larger reasonable specific surface area (351 $m^2\ g^{-1}$) of the carbon matrix not only ensure sufficient electrolyte/electrode contact, but also offer expanded space to serve as a cushion for volumetric variation in the repeated charge-discharge processes. (iii) The nitrogen-doped nanostructure supplies more active sites

for storing $Li^+/Na^+/K^+$, and provides a vital pseudocapacitance effect. As shown in **Figure S5**, the ZVO/NC electrode maintains its polyhedral structure without a visible large range of aggregations after cycling for 50 cycles, while the ZVO/ZO/NC electrode shows large aggregations and obvious pulverization, indicating the high structural stability of the ZVO/NC electrode. This novel architecture and suitable electrolyte surmount the depressed reaction kinetics and relieve the volume changes that occur during the electrochemical process in LIBs/SIBs, and even in PIBs.

4. Conclusions

In summary, a self-assembly strategy followed by *in situ* pyrolysis was developed to fabricate Zn_2VO_4 nanoparticles encapsulated in the an N-doped nanocarbon network, which were derived from a V/Zn-MOF precursor. Compared to previous higher-costly strategies (such as solvothermal method) to synthesize bimetallic vanadate material [30, 33], we utilized a convenient ZIF-8 self-assembly route, placing V species into suitable cavities to form zinc vanadate polyhedron. The adopted N-doped carbon encapsulated Zn_2VO_4 polyhedron, which display a uniform size distribution of approximately 100-300 nm and a larger specific surface area (351 $m^2 g^{-1}$), tends to improve the diffusion kinetics, favors enhanced electrochemical behaviour. When evaluated as an anode material for alkali ion batteries, ZVO/NC exhibits superior electrochemical performance. In particular, it delivers a superior reversible capacity (807 mAh g^{-1} after 200 cycles at 0.5 A g^{-1}) for LIBs, and presents an ultralong cycling performance (145 mAh g^{-1} after 7000 cycles at 2.0 A g^{-1}) for SIBs. It also shows excellent cycle stability (140 mAh g^{-1} after 1000 cycles at 0.5 A g^{-1}) for PIBs. We also investigated different

electrolytes for SIBs and PIBs, which provided suggestions for bimetallic oxide electrodes. Inspired by such strategy, series of advanced bimetallic oxide electrodes can be tailored and applied for other energy storage fields such as Li-S batteries, aqueous Zn-ion batteries, and supercapacitors.

Acknowledgements

This work was financially supported by National Natural Science Foundation of China (NSFC 51502036 and 21875037), National Key R&D Program of China (2019YFC1904500), the New Century Talent Project of Fujian Province and Natural Science Foundation of Distinguished Young Scholars for Fujian Province (2019J06015).

Conflict of interests

The authors declare no conflict of interests.

References

[1] B. Dunn, H. Kamath, J.M. Tarascon, Electrical energy storage for the grid: a battery of choices, Science 334 (2011) 928-935.

[2] J.B. Goodenough, Y. Kim, Challenges for rechargeable Li batteries, Chem Mater. 22 (2010) 587-603.

[3] Y. Sun, S. Guo, H. Zhou, Exploration of advanced electrode materials for rechargeable sodium-ion batteries, Adv. Energy Mater. 9 (2019) 1800212.

[4] J.Y. Hwang, S.T. Myung, Y.K. Sun, Sodium-ion batteries: present and future, Chem. Soc. Rev. 46 (2017) 3529-3614.

[5] H. Kim, J.C. Kim, M. Bianchini, D.-H. Seo, J. Rodriguez-Garcia, G. Ceder, Recent

progress and perspective in electrode materials for K-ion Batteries, Adv. Energy Mater. 8 (2018) 1702384.

[6] M. Zheng, H. Tang, L. Li, Q. Hu, L. Zhang, H. Xue, H. Pang, Hierarchically nanostructured transition metal oxides for lithium-Ion Batteries, Adv. Sci. 5 (2018) 1700592.

[7] X. Yao, Y. Ke, W. Ren, X. Wang, F. Xiong, W. Yang, M. Qin, Q. Li, L. Mai, Defect-rich soft carbon porous nanosheets for fast and high-capacity sodium-ion storage, Adv. Energy Mater. 9 (2018) 1803260.

[8] Z. Jian, S. Hwang, Z. Li, A.S. Hernandez, X. Wang, Z. Xing, D. Su, X. Ji, Hard-soft composite carbon as a long-cycling and high-rate anode for potassium-ion batteries, Adv. Funct. Mater. 27 (2017) 1700324.

[9] Y. Lu, L. Yu, M. Wu, Y. Wang, X.W.D. Lou, Construction of complex Co_3O_4 @$Co_3V_2O_8$ hollow structures from metal-organic frameworks with enhanced lithium storage properties, Adv. Mater. 30 (2018) 1702875.

[10] Y. Yang, M. Luo, Y. Xing, S. Wang, W. Zhang, F. Lv, Y. Li, Y. Zhang, W. Wang, S. Guo, A universal strategy for intimately coupled carbon nanosheets/MoM nanocrystals (M = P, S, C, and O) hierarchical hollow nanospheres for hydrogen hvolution catalysis and sodium-ion storage, Adv. Mater. 30 (2018) 1706085.

[11] Z. Huang, H. Hou, C. Wang, S. Li, Y. Zhang, X. Ji, Molybdenum phosphide: a conversion-type anode for ultralong-life sodium-ion batteries, Chem. Mater. 29 (2017) 7313-7322.

[12] Y. Liu, N. Zhang, C. Yu, L. Jiao, J. Chen, $MnFe_2O_4$@C nanofibers as high-

performance anode for sodium-ion batteries, Nano Lett. 16 (2016) 3321-3328.

[13] Y. Mo, Q. Ru, J. Chen, X. Song, L. Guo, S. Hu, S. Peng, Three-dimensional $NiCo_2O_4$ nanowire arrays: preparation and storage behavior for flexible lithium-ion and sodium-ion batteries with improved electrochemical performance, J. Mater. Chem. A 3 (2015) 19765-19773.

[14] Q. He, S. Gu, T. Wu, S. Zhang, X. Ao, J. Yang, Z. Wen, Self-supported mesoporous $FeCo_2O_4$ nanosheets as high capacity anode material for sodium-ion battery, Chem. Eng. J. 330 (2017) 764-773.

[15] X. Wang, K. Cao, Y. Wang, L. Jiao, Controllable N-Doped $CuCo_2O_4$@C film as a self-supported anode for ultrastable sodium-ion batteries, Small 13 (2017) 1700873.

[16] M. Mao, C. Cui, M. Wu, M. Zhang, T. Gao, X. Fan, J. Chen, T. Wang, J. Ma, C. Wang, Flexible ReS_2 nanosheets/N-doped carbon nanofibers-based paper as a universal anode for alkali (Li, Na, K) ion battery, Nano Energy 45 (2018) 346-352.

[17] W. Zhang, W.K. Pang, V. Sencadas, Z. Guo, Understanding high-energy-density Sn_4P_3 anodes for potassium-ion batteries, Joule 2 (2018) 1534-1547.

[18] G. Wang, X. Xiong, D. Xie, Z. Lin, J. Zheng, F. Zheng, Y. Li, Y. Liu, C. Yang, M. Liu, Chemically activated hollow carbon nanospheres as a high-performance anode material for potassium ion batteries, J. Mater. Chem. A 6 (2018) 24317-24323.

[19] C. Zhu, Z. Liu, J. Wang, J. Pu, W. Wu, Q. Zhou, H. Zhang, Novel Co_2VO_4 anodes using ultralight 3D metallic current collector and carbon sandwiched structures for high-performance Li-ion batteries, Small 13 (2017) 1701260.

[20] C. Lv, J. Sun, G. Chen, C. Yan, D. Chen, Achieving $Ni_3V_2O_8$ amorphous wire

encapsulated in crystalline tube nanostructure as anode materials for lithium ion batteries, Nano Energy 33 (2017) 138-145.

[21] X. Xu, P. Wu, Q. Li, W. Yang, X. Zhang, X. Wang, J. Meng, C. Niu, L. Mai, Realizing stable lithium and sodium storage with high areal capacity using novel nanosheet-assembled compact CaV_4O_9 microflowers, Nano Energy 50 (2018) 606-614.

[22] X. Niu, Y. Zhang, L. Tan, Z. Yang, J. Yang, T. Liu, L. Zeng, Y. Zhu, L. Guo, Amorphous $FeVO_4$ as a promising anode material for potassium-ion batteries, Energy Storage Mater. 22 (2019) 160-167.

[23] B. Sambandam, V. Soundharrajan, J. Song, S. Kim, J. Jo, P.T. Duong, S. Kim, V. Mathew, J. Kim, Investigation of Li-ion storage properties of earth abundant β-$Mn_2V_2O_7$ prepared using facile green strategy, J. Power Sources 350 (2017) 80-86.

[24] L. Xiao, Y. Zhao, J. Yin, L. Zhang, Clewlike ZnV_2O_4 hollow spheres: nonaqueous sol-gel synthesis, formation mechanism, and lithium storage properties, Chem. Eur. J. 15 (2009) 9442-9450.

[25] F.K. Butt, C. Cao, Q. Wan, P. Li, F. Idrees, M. Tahir, W.S. Khan, Z. Ali, M.J.M. Zapata, M. Safdar, X. Qu, Synthesis, evolution and hydrogen storage properties of ZnV_2O_4 glomerulus nano/microspheres: A prospective material for energy storage, Int. J. Hydrogen Energ. 39 (2014) 7842-7851.

[26] B. Sambandam, V. Soundharrajan, J. Song, S. Kim, J. Jo, D.T. Pham, S. Kim, V. Mathew, J. Kim, $Zn_3V_2O_8$ porous morphology derived through a facile and green approach as an excellent anode for high-energy lithium ion batteries, Chem. Eng. J. 328 (2017) 454-463.

[27] R. Nie, G. Fang, J. Zhou, J. Guo, Y. Tang, S. Liu, Y. Cai, P. Hao, S. Liang, Three-dimensional $Zn_3V_3O_8$/carbon fiber cloth composites as binder-free anode for lithium-ion batteries, Electrochim. Acta 246 (2017) 97-105.

[28] C. Bie, J. Pei, G. Chen, Q. Zhang, J. Sun, Y. Yu, D. Chen, Hierarchical $Zn_3V_3O_8$/C composite microspheres assembled from unique porous hollow nanoplates with superior lithium storage capability, J. Mater. Chem. A 4 (2016) 17063-17072.

[29] L. Zeng, F. Xiao, J. Wang, S. Gao, X. Ding, M. Wei, ZnV_2O_4–CMK nanocomposite as an anode material for rechargeable lithium-ion batteries, J. Mater. Chem. 22 (2012) 14284-14288.

[30] H. Xue, Y. Fang, L. Zeng, X. He, F. Luo, R. Liu, J. Liu, Q. Chen, M. Wei, Q. Qian, Facile synthesis of hierarchical lychee-like $Zn_3V_3O_8$@C/rGO nanospheres as high-performance anodes for lithium ion batteries, J. Colloid Interf. Sci. 533 (2018) 627-635.

[31] Y. Sun, C.-S. Li, Q.-R. Yang, S.-L. Chou, H.-K. Liu, Electrochemically active, novel layered m-ZnV_2O_6 nanobelts for highly rechargeable Na-ion energy storage, Electrochim. Acta 205 (2016) 62-69.

[32] I.V.B. Maggay, L.M.Z. De Juan, M.T. Nguyen, T. Yonezawa, B.K. Chang, T.S. Chan, W.-R. Liu, ZnV_2O_4 : A potential anode material for sodium-ion batteries, J. Taiwan Inst. Chem. E. 88 (2018) 161-168.

[33] S. Cheng, Q. Ru, Z. Shi, Y. Gao, Y. Liu, X. Hou, F. Chen, F.C.-C. Ling, Plant oil–inspired 3D flower-like $Zn_3V_3O_8$ nanospheres coupled with N-Doped carbon as anode material for Li-/Na-ion batteries, Energy Technology 7 (2019) 1900754.

[34] R. Muruganantham, I.V.B. Maggay, L.M.Z.D. Juan, M.T. Nguyen, T. Yonezawa,

C.-H. Lin, Y.-G. Lin, W.-R. Liu, Electrochemical exploration of the effects of calcination temperature of a mesoporous zinc vanadate anode material on the performance of Na-ion batteries, Inorg. Chem. Front. 6 (2019) 2653-2659.

[35] X. Cao, C. Tan, M. Sindoro, H. Zhang, Hybrid micro-/nano-structures derived from metal-organic frameworks: preparation and applications in energy storage and conversion, Chem. Soc. Rev. 46 (2017) 2660-2677.

[36] G. Zou, H. Hou, P. Ge, Z. Huang, G. Zhao, D. Yin, X. Ji, Metal-organic framework-derived materials for sodium energy storage, Small 14 (2018) 1702648.

[37] X.-C. Xie, K.-J. Huang, X. Wu, Metal-organic framework derived hollow materials for electrochemical energy storage, J. Mater. Chem. A 6 (2018) 6754-6771.

[38] C. Wang, Y.V. Kaneti, Y. Bando, J. Lin, C. Liu, J. Li, Y. Yamauchi, Metal–organic framework-derived one-dimensional porous or hollow carbon-based nanofibers for energy storage and conversion, Mater. Horiz. 5 (2018) 394-407.

[39] Q. Yang, Q. Xu, H.L. Jiang, Metal-organic frameworks meet metal nanoparticles: synergistic effect for enhanced catalysis, Chem. Soc. Rev. 46 (2017) 4774-4808.

[40] L. Zhang, T. Mi, M.A. Ziaee, L. Liang, R. Wang, Hollow POM@MOF hybrid-derived porous $Co_3O_4/CoMoO_4$ nanocages for enhanced electrocatalytic water oxidation, J. Mater. Chem. A 6 (2018) 1639-1647.

[41] S. Dong, C. Li, X. Ge, Z. Li, X. Miao, L. Yin, ZnS-Sb_2S_3@C core-double shell polyhedron structure derived from metal-organic framework as anodes for high performance sodium ion batteries, ACS Nano 11 (2017) 6474-6482.

[42] T. Yang, Y. Liu, Z. Huang, J. Liu, P. Bian, C.D. Ling, H. Liu, G. Wang, R. Zheng,

In situ growth of ZnO nanodots on carbon hierarchical hollow spheres as high-performance electrodes for lithium-ion batteries, J. Alloy Compd. 735 (2018) 1079-1087.

[43] M. Wang, M. Lin, J. Li, L. Huang, Z. Zhuang, C. Lin, L. Zhou, L. Mai, Metal-organic framework derived carbon-confined Ni_2P nanocrystals supported on graphene for an efficient oxygen evolution reaction, Chem. Commun. 53 (2017) 8372-8375.

[44] N.L. Torad, M. Hu, Y. Kamachi, K. Takai, M. Imura, M. Naito, Y. Yamauchi, Facile synthesis of nanoporous carbons with controlled particle sizes by direct carbonization of monodispersed ZIF-8 crystals, Chem. Commun. 49 (2013) 2521-2523.

[45] Q. Liu, J.M. Yang, L.N. Jin, W.Y. Sun, Controlled synthesis of porous coordination-polymer microcrystals with definite morphologies and sizes under mild conditions, Chem. Eur. J. 20 (2014) 14783-14789.

[46] F. Zou, X. Hu, Z. Li, L. Qie, C. Hu, R. Zeng, Y. Jiang, Y. Huang, MOF-derived porous $ZnO/ZnFe_2O_4$/C octahedra with hollow interiors for high-rate lithium-ion batteries, Adv. Mater. 26 (2014) 6622-6628.

[47] J. Zhou, B. Zhao, J. Bai, Z. Fang, K. Li, H. Ma, J. Dai, X. Zhu, Y. Sun, Three-dimensional porous Zn_2VO_4/ZnO/C thin film anode materials for high-performance Li-ion batteries, Scripta Mater. 166 (2019) 87-91.

[48] M. Zhu, Z. Luo, A. Pan, H. Yang, T. Zhu, S. Liang, G. Cao, N-doped one-dimensional carbonaceous backbones supported $MoSe_2$ nanosheets as superior electrodes for energy storage and conversion, Chem. Eng. J. 334 (2018) 2190-2200.

[49] C. Yang, F. Lv, Y. Zhang, J. Wen, K. Dong, H. Su, F. Lai, G. Qian, W. Wang, A.

Hilger, Y. Xu, Y. Zhu, Y. Deng, W. Hu, I. Manke, Y. Chen, Confined Fe_2VO_4 ⊂Nitrogen-doped carbon nanowires with internal void Sspace for high-rate and ultrastable potassium-ion storage, Adv. Energy Mater. 9 (2019) 1902674.

[50] Q. Zhang, J. Pei, G. Chen, C. Bie, J. Sun, J. Liu, Porous $Co_3V_2O_8$ nanosheets with ultrahigh performance as anode materials for lithium ion batteries, Adv. Mater. Interf. 4 (2017) 1700054.

[51] Q. Zhang, J. Pei, G. Chen, C. Bie, D. Chen, Y. Jiao, J. Rao, $Co_3V_2O_8$ hexagonal pyramid with tunable inner structure as high performance anode materials for lithium ion battery, Electrochim. Acta 238 (2017) 227-236.

[52] C. Bie, J. Pei, J. Wang, K. Hua, D. Chen, G. Chen, Graphite nanoplates firmly anchored with well-dispersed porous $Zn_3V_2O_8$ nanospheres: rational fabrication and enhanced lithium storage capability, Electrochim. Acta 248 (2017) 140-149.

[53] Z. Zhang, Y. Huang, X. Liu, C. Chen, Z. Xu, P. Liu, Zeolitic imidazolate frameworks derived ZnS/Co_3S_4 composite nanoparticles doping on polyhedral carbon framework for efficient lithium/sodium storage anode materials. Carbon 157 (2020) 244-254.

[54] L. Xu, P. Xiong, L. Zeng, Y. Fang, R. Liu, J. Liu, F. Luo, Q. Chen, M. Wei, Q. Qian, Electrospun $VSe_{1.5}$/CNF composite with excellent performance for alkali metal ion batteries, Nanoscale 11 (2019) 16308-16316.

[55] X. Hu, X. Liu, K. Chen, G. Wang, H. Wang, Core–shell MOF-derived N-doped yolk–shell carbon nanocages homogenously filled with ZnSe and $CoSe_2$ nanodots as excellent anode materials for lithium- and sodium-ion batteries, J. Mater. Chem. A 7

(2019) 11016-11037.

[56] G. Zou, H. Hou, G. Zhao, P. Ge, D. Yin, X. Ji, N-rich carbon coated $CoSnO_3$ derived from in situ construction of a Co–MOF with enhanced sodium storage performance, J. Mater. Chem. A 6 (2018) 4839-4847.

[57] H. Yan, Y. Luo, X. Xu, L. He, J. Tan, Z. Li, X. Hong, P. He, L. Mai, Facile and scalable synthesis of $Zn_3V_2O_7(OH)_2$•$2H_2O$ microflowers as a high-performance anode for lithium-ion batteries, ACS Appl. Mater. Inter. 9 (2017) 27707-27714.

[58] G. Yang, S. Li, M. Wu, C. Wang, Zinc pyrovanadate nanosheets of atomic thickness: excellent Li-storage properties and investigation of their electrochemical mechanism, J. Mater. Chem. A 4 (2016) 10974-10985.

[59] Y. Bai, Y. Tang, Y. Gao, X. Li, L. Liu, Y. Zhang, S. Gao, Bamboo-like porous CNTs encapsulated $Zn_3V_3O_8$ nanoparticles as high-performance anodes for lithium ion batteries, J. Alloys Compd. 798 (2019) 678-684.

[60] C. Zheng, L. Zeng, M. Wang, H. Zheng, M. Wei, Synthesis of hierarchical ZnV_2O_4 microspheres and its electrochemical properties, CrystEngComm 16 (2014) 10309-10313.

[61] Z. Shi, Q. Ru, S. Cheng, X. Hou, F. Chen, F. C.-C. Ling, Hierarchically rambutan-like $Zn_3V_3O_8$ hollow spheres as anodes for lithium-/potassium-ion batteries, Energy Technology 8 (2020) 2000010.

[62] T. Brezesinski, J. Wang, J. Polleux, B. Dunn, S.H. Tolbert, Templated nanocrystal-based porous TiO_2 films for next-generation electrochemical capacitors, J. Am. Chem. Soc. 131 (2009) 1802-1809.

[63] V. Augustyn, J. Come, M.A. Lowe, J.W. Kim, P.L. Taberna, S.H. Tolbert, H.D. Abruna, P. Simon, B. Dunn, High-rate electrochemical energy storage through Li^+ intercalation pseudocapacitance, Nat. Mater. 12 (2013) 518-522.

[64] G. Fang, Z. Wu, J. Zhou, C. Zhu, X. Cao, T. Lin, Y. Chen, C. Wang, A. Pan, S. Liang, Observation of pseudocapacitive effect and fast ion diffusion in bimetallic sulfides as an advanced sodium-ion battery anode, Adv. Energy Mater. 8 (2018) 1703155.

[65] C. Bommier, X. Ji, Electrolytes, SEI formation, and binders: a review of nonelectrode factors for sodium-ion battery anodes, Small 14 (2018) 1703576.

[66] L. Deng, Y. Zhang, R. Wang, M. Feng, X. Niu, L. Tan, Y. Zhu, Influence of KPF_6 and KFSI on the performance of anode materials for potassium-ion batteries: a case study of MoS_2, ACS Appl. Mater. Inter. 11 (2019) 22449-22456.

[67] Q. Tan, W. Zhao, K. Han, P. Li, W. Wang, D. He, Z. Liu, Q. Yu, M. Qin, X. Qu, The multi-yolk/shell structure of FeP@foam-like graphenic scaffolds: strong P–C bonds and electrolyte- and binder-optimization boost potassium storage, J. Mater. Chem. A 7 (2019) 15673-15682.

[68] Z. Qin, C. Lv, J. Pei, C. Yan, Y. Hu, G. Chen, A 1D Honeycomb-like amorphous zincic vanadate for stable and fast sodium-ion storage, Small 16 (2020) 1906214.

[69] X. Xu, C. Niu, M. Duan, X. Wang, L. Huang, J. Wang, L. Pu, W. Ren, C. Shi, J. Meng, B. Song, L. Mai, Alkaline earth metal vanadates as sodium-ion battery anodes, Nat. Commun. 8 (2017) 1-11.

[70] L.M.Z. De Juan-Corpuz, M.T. Nguyen, R.D. Corpuz, T. Yonezawa, N.C. Rosero-

Navarro, K. Tadanaga, T. Tokunaga, S. Kheawhom, Porous ZnV_2O_4 nanowire for stable and high-rate lithium-ion battery anodes, ACS Appl. Nano Mater. 2 (2019) 4247-4256.

[71] Y. Fang, R. Liu, L. Zeng, J. Liu, L. Xu, X. He, B. Huang, Q. Chen, M. Wei, Q. Qian, Preparation of Ge/N, S co-doped ordered mesoporous carbon composite and its long-term cycling performance of lithium-ion batteries, Electrochim. Acta 318 (2019) 737-745.

[72] P. Hu, X. Wang, T. Wang, L. Chen, J. Ma, Q. Kong, S. Shi, G. Cui, Boron substituted $Na_3V_2(P_{1-x}B_xO_4)_3$ cathode materials with enhanced performance for sodium-ion batteries, Adv. Sci. 3 (2016) 1600112.

Figure captions

Scheme 1 Preparation of ZVO/ZO/NC and ZVO/NC nanocomposites.

Figure 1. (a) XRD patterns and (b) Raman spectra of ZVO/NC and ZVO/ZO/NC samples; (c) TG curves of ZVO/NC samples; (d) N_2 adsorption–desorption isotherms and pore size distributions (insert) of ZVO/NC samples.

Figure 2. (a) Survey spectra, (b) Zn 2p, (c) V 2p, (d) O 1s, (e) C 1s and (f) N 1s high-resolution XPS spectra of the ZVO/NC sample; (g) graphical presentation of the configurations and contents of three types of N in the ZVO/NC sample.

Figure 3. (a-b) SEM and (c-e) HR-TEM images of the ZVO/NC composite; (f) Elemental mapping results of ZVO/NC.

Figure 4. Electrochemical performance of LIBs: (a) Cyclic voltammetry curves of ZVO/NC at a scan rate of 0.1 mV s^{-1}; (b) Charge-discharge profiles of ZVO/NC at 0.5 A g^{-1} within a voltage range of 0.01-3.0 V; (c) The cycling performance of ZVO/NC and ZVO/ZO/NC electrodes at a current density of 0.5 A g^{-1}; (d) The rate capability of ZVO/NC and ZVO/ZO/NC electrodes at different current densities between 0.5 and 8.0 A g^{-1}. (e) Long-term cycling performance of ZVO/NC and ZVO/ZO/NC electrodes at 5.0 A g^{-1} and coulombic efficiency of the ZVO/NC electrode.

Figure 5. (a) Cyclic voltammetry curves of the ZVO/NC electrode for LIBs at different scan rates from 0.2 to 10.0 mV s^{-1}; (b) log(i) versus log(v) plots at different oxidation and reduction peaks; (c) Capacitive contribution (pink area) of ZVO/NC at 1.0 mV s^{-1}; (d) The diffusion controlled (green) and capacitive (pink) capacities of ZVO/NC at different scan rates.

Figure 6. Electrochemical performance of SIBs: (a) Comparison of cycling performances of ZVO/NC electrodes at 0.1 A g^{-1}over 50 cycles using 1.0 M $NaPF_6$, 1.0

M $NaClO_4$ and 1.0 M $NaCF_3SO_3$ as the electrolyte; (b) The cycling performance of the ZVO/NC and ZVO/ZO/NC electrodes at a current density of 0.1 A g^{-1}; (c) The cycling performance of ZVO/NC and ZVO/ZO/NC electrodes at 1.0 A g^{-1} and the coulombic efficiency of the ZVO/NC electrode; (d) The coulombic efficiency and long-term cycling performance of the ZVO/NC electrode at a high current density of 2.0 A g^{-1}.

Figure 7. (a) Cyclic voltammetry curves of the ZVO/NC electrode for SIBs at different scan rates from 0.2 to 1.0 mV s^{-1}; (b) Log(*i*) versus log(*v*) plots at different oxidation and reduction peaks; (c) capacitive contribution (pink area) of ZVO/NC at 1.0 mV s^{-1}; (d) diffusion controlled (green) and capacitive (pink) capacities of ZVO/NC at different scan rates.

Figure 8. Electrochemical performance of PIBs: (a) Comparison of cycling performances of ZVO/NC electrodes at 0.1 A g^{-1}over 50 cycles using 1.0 M KPF_6 in ester or ether-type organic solvents as the electrolytes, respectively; (b) The cycling performance of ZVO/NC and ZVO/ZO/NC electrodes at a current density of 0.1 A g^{-1}; (c) The coulombic efficiency and long-term cycling performance of the ZVO/NC electrode at a high current density of 0.5 A g^{-1} ; (d) Cyclic voltammetry curves of the ZVO/NC electrode for PIBs at different scan rates from 0.2 to 1.0 mV s^{-1}; (e) Log(*i*) versus log(*v*) plots at different oxidation and reduction peaks; (f) capacitive contribution (pink area) of ZVO/NC at 1.0 mV s^{-1}; (g) diffusion controlled (green) and capacitive (pink) capacities of ZVO/NC at different scan rates.

Figure 9. EIS spectra of the ZVO/NC electrode before and after 5 cycles at a current density of 0.5 A g^{-1} for LIBs, SIBs and PIBs, respectively.

Scheme 2 (a) Schematic illustration of the excellent structural stability of the ZVO/NC nanocomposite; (b) Schematic illustrations of the degradation mechanisms, and the morphology evolution during the charge/discharge process in the ZVO/NC electrode

(taking intercalation/deintercalation of lithium as an example).

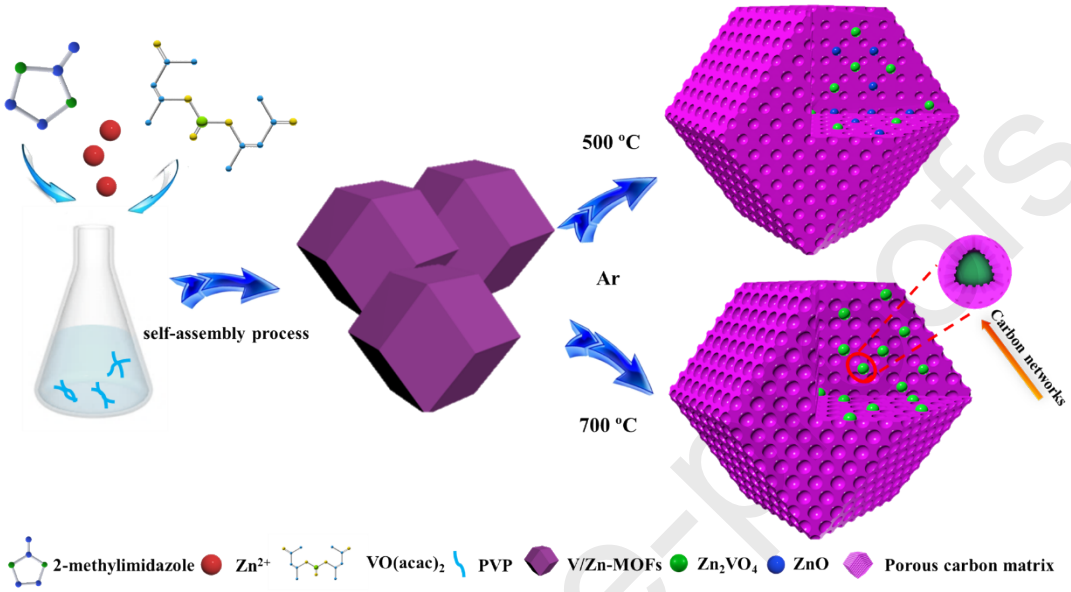

Scheme 1

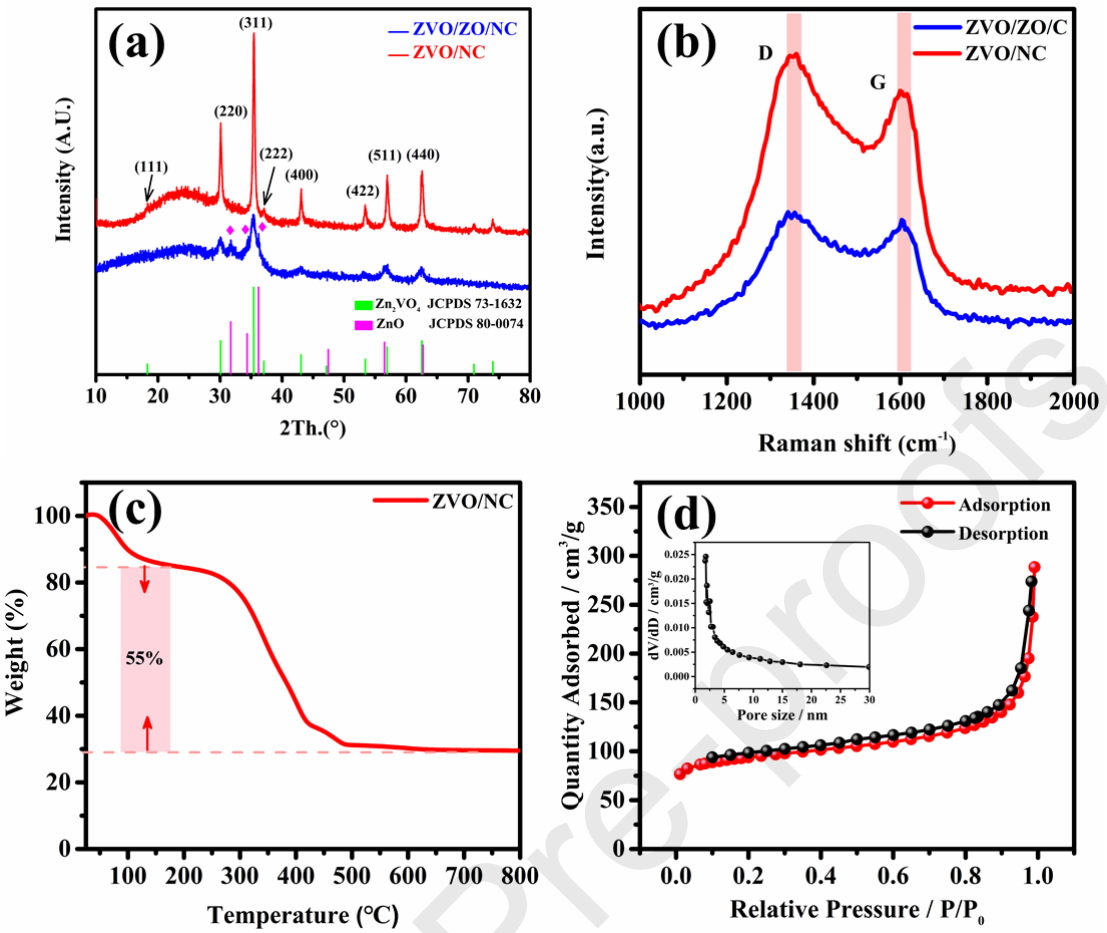

Figure 1

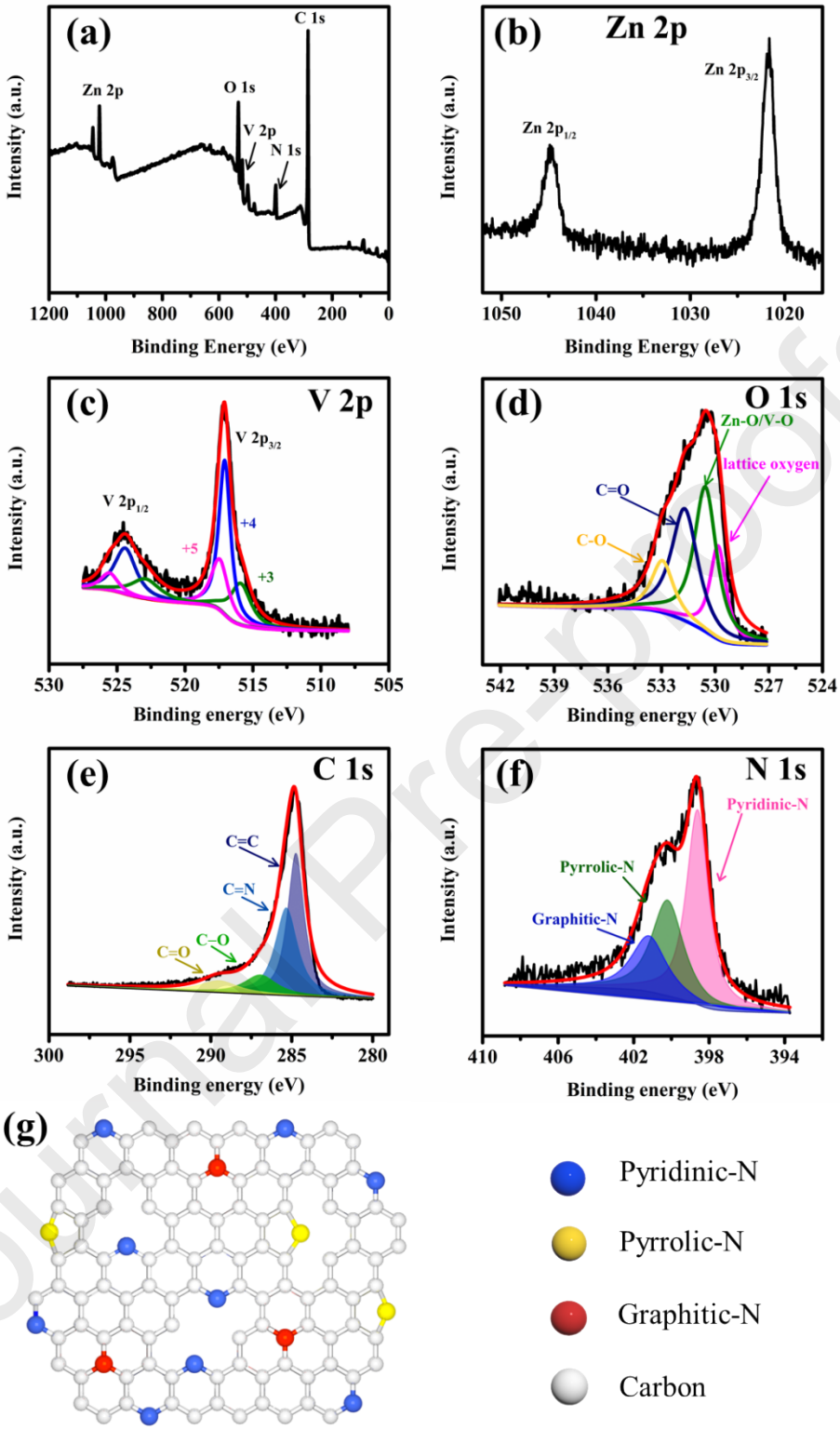

N-Types	Pyridinic-N	Pyrrolic-N	Graphitic-N
Content (wt.%)	49.4%	30.1%	20.5%

Figure 2

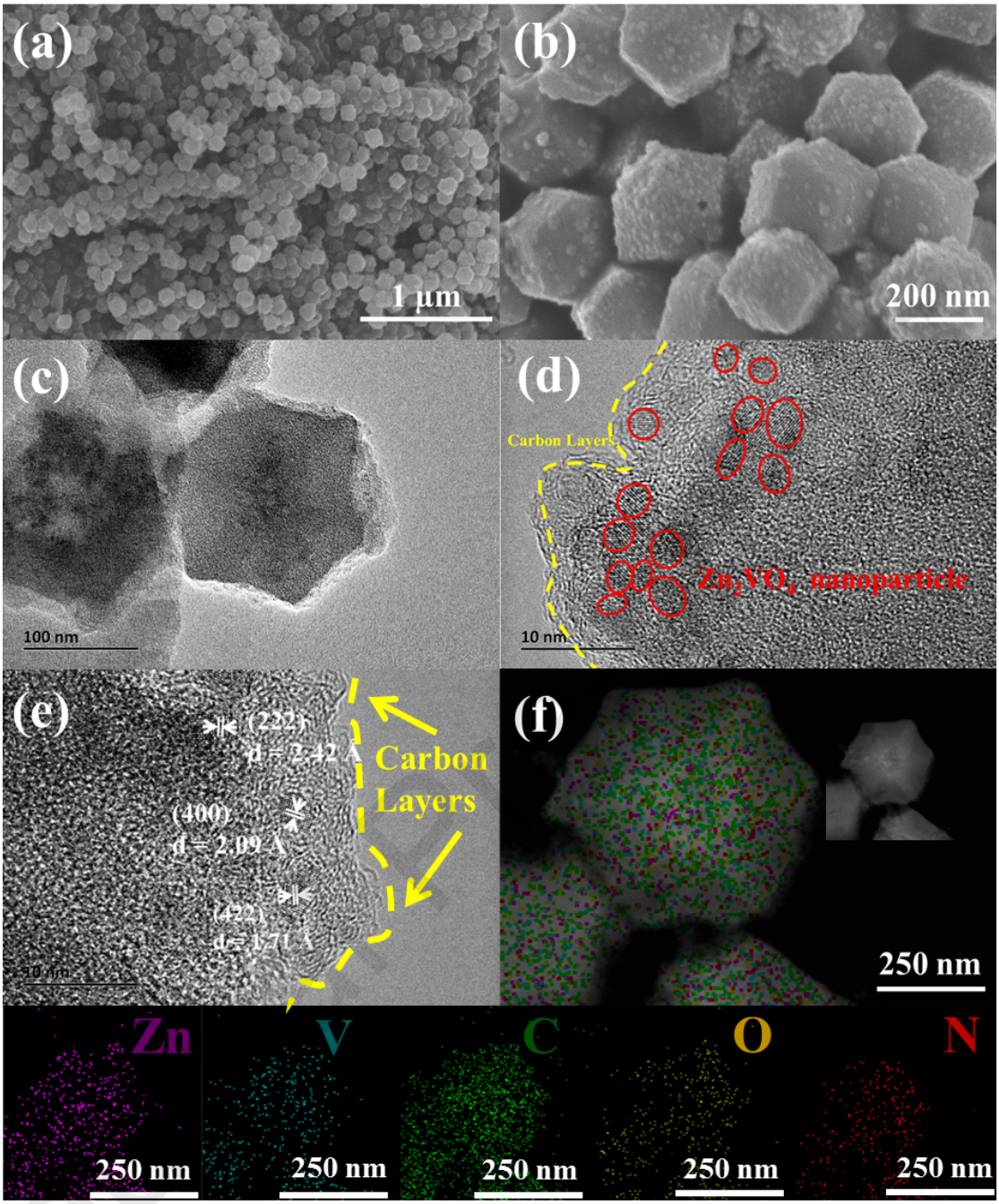
(a)
1 μm
(b)
200 nm
(c)
100 nm
(d)
Carbon Layers
Zn_2VO_4 nanoparticle
10 nm
(e)
(222)
d = 2.42 Å
(400)
d = 2.09 Å
(422)
d = 1.71 Å
Carbon Layers
10 nm
(f)
250 nm
Zn
V
C
O
N
250 nm
250 nm
250 nm
250 nm
250 nm

Figure 3

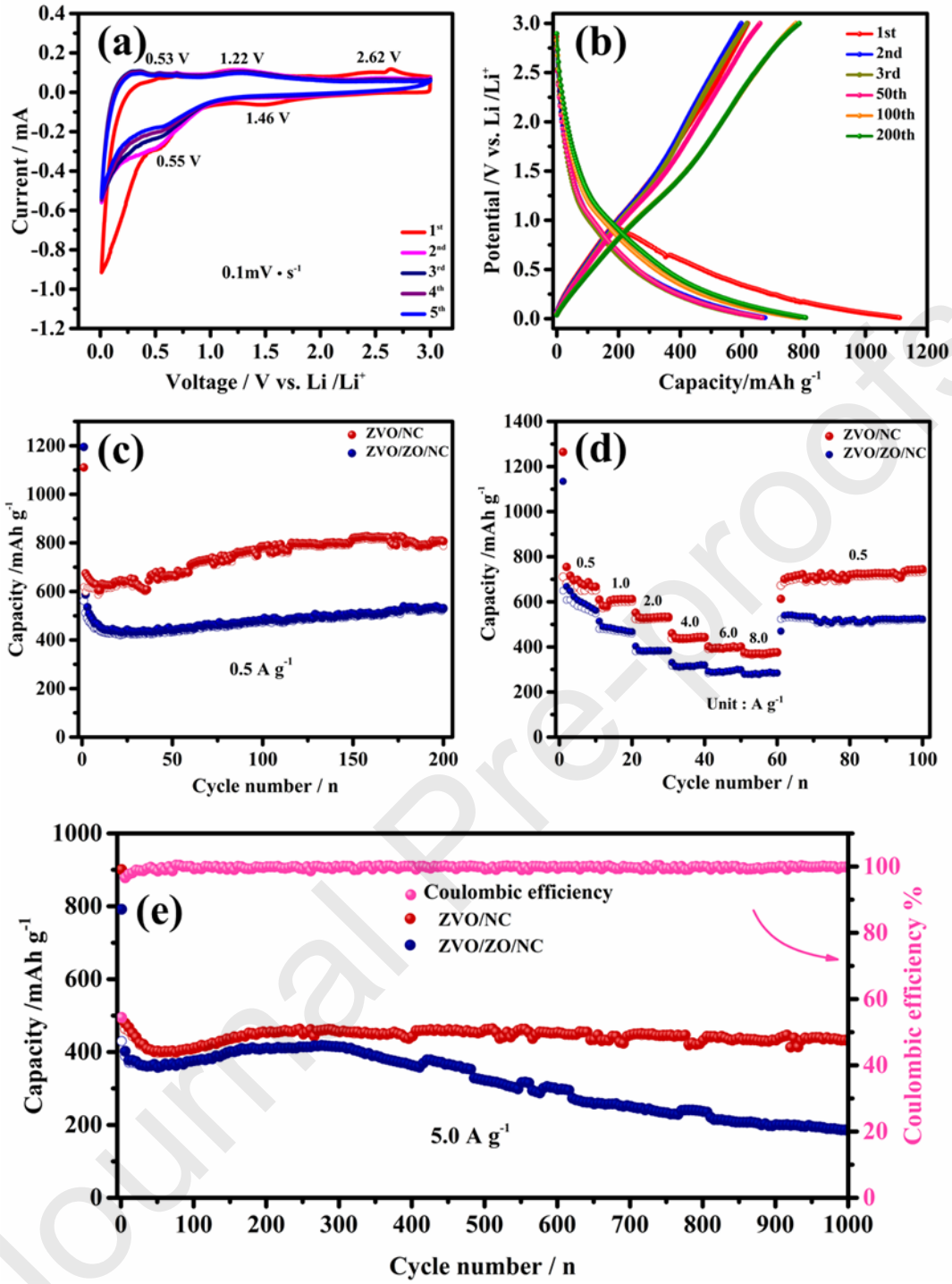

Figure 4

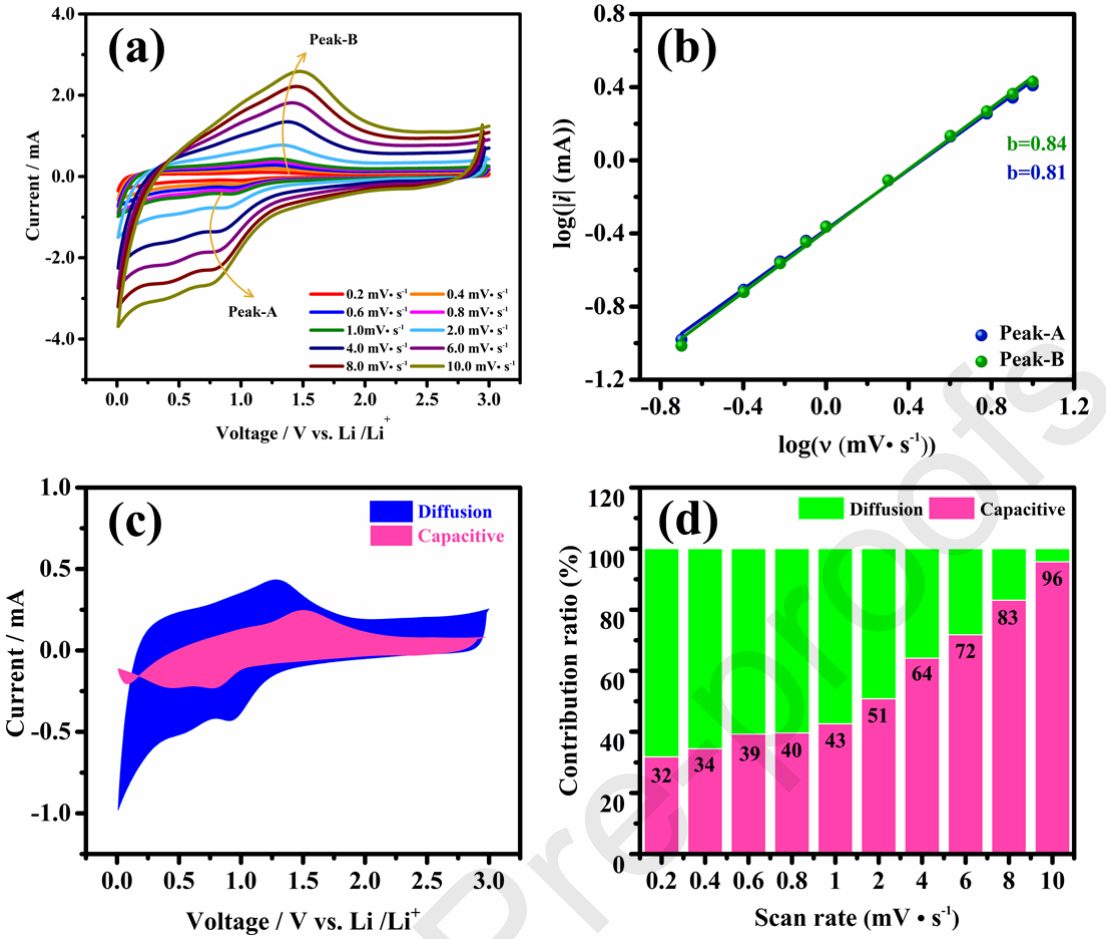

Figure 5

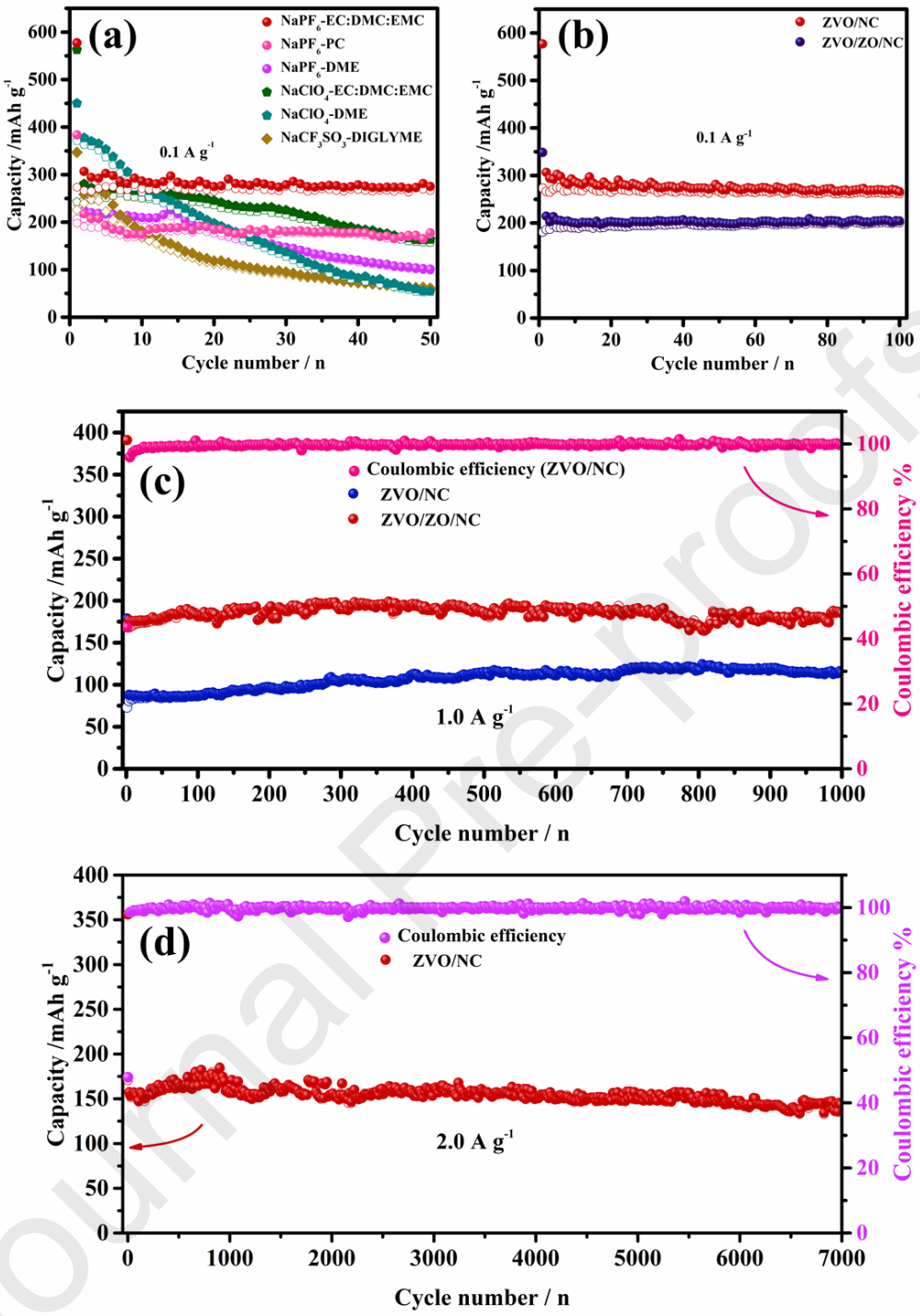

Figure 6

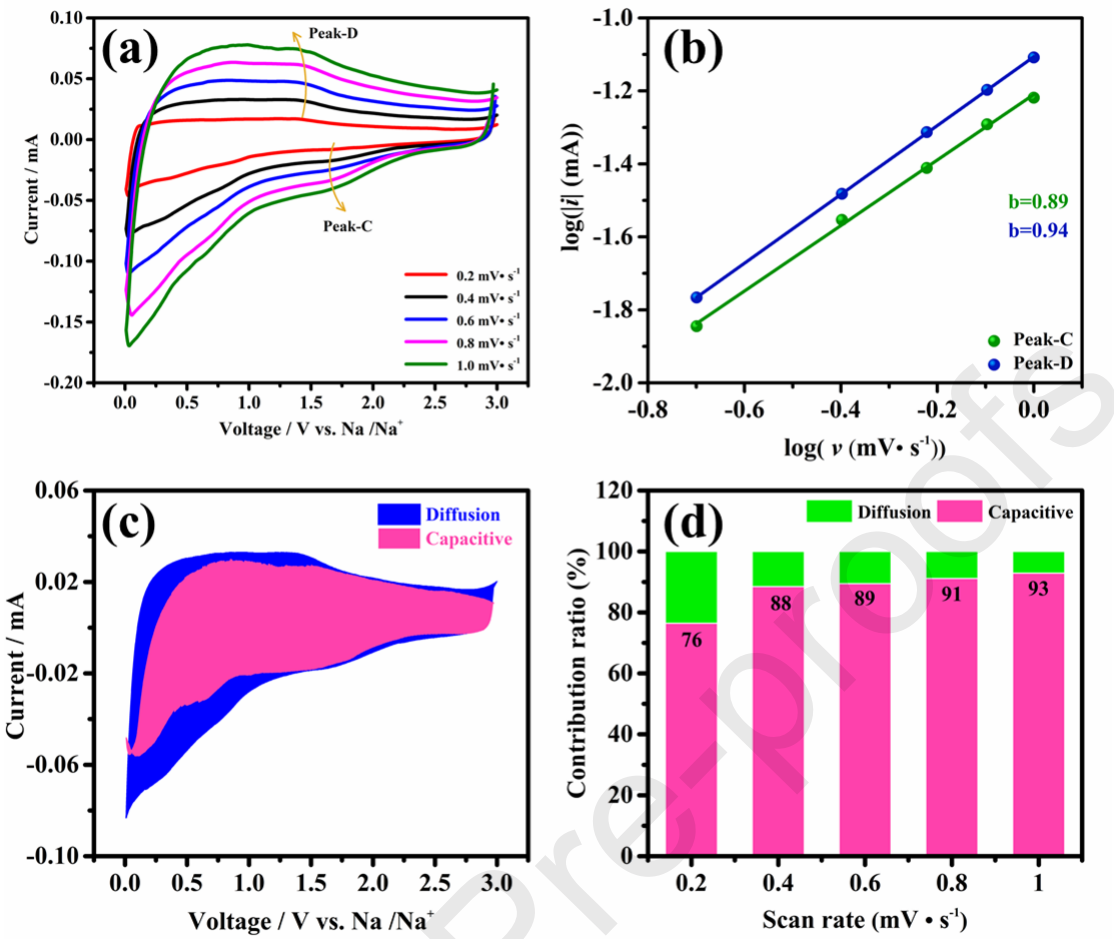

Figure 7

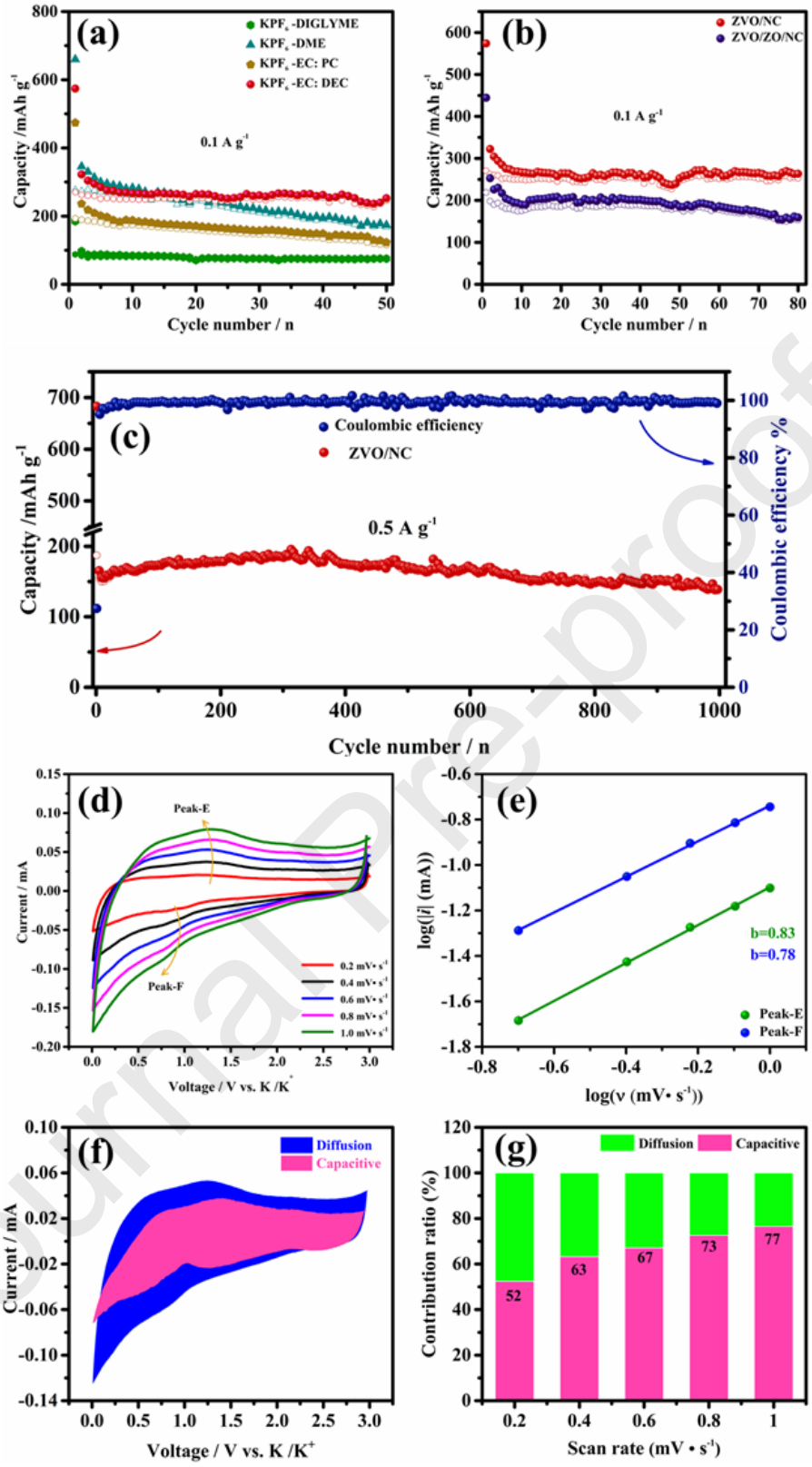
(a)
KPF6-DIGLYME
KPF6-DME
KPF6-EC: PC
KPF6-EC: DEC
0.1 A g-1
Capacity /mAh g-1
Cycle number / n
(b)
ZVO/NC
ZVO/ZO/NC
0.1 A g-1
Capacity /mAh g-1
Cycle number / n
(c)
Coulombic efficiency
ZVO/NC
0.5 A g-1
Capacity /mAh g-1
Coulombic efficiency %
Cycle number / n
(d)
Peak-E
Peak-F
0.2 mV• s-1
0.4 mV• s-1
0.6 mV• s-1
0.8 mV• s-1
1.0 mV• s-1
Current / mA
Voltage / V vs. K /K+
(e)
b=0.83
b=0.78
Peak-E
Peak-F
log(|i|) (mA))
log(v (mV• s-1))
(f)
Diffusion
Capacitive
Current / mA
Voltage / V vs. K /K+
(g)
Diffusion
Capacitive
52
63
67
73
77
Contribution ratio (%)
Scan rate (mV • s-1)

Figure 8

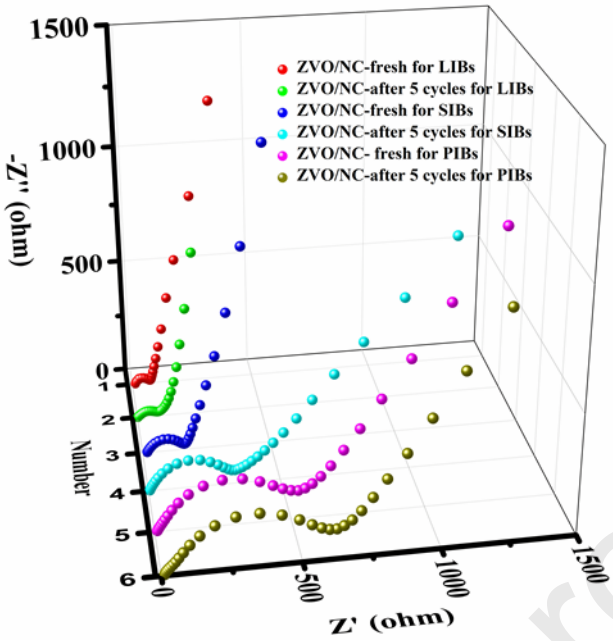

Figure 9

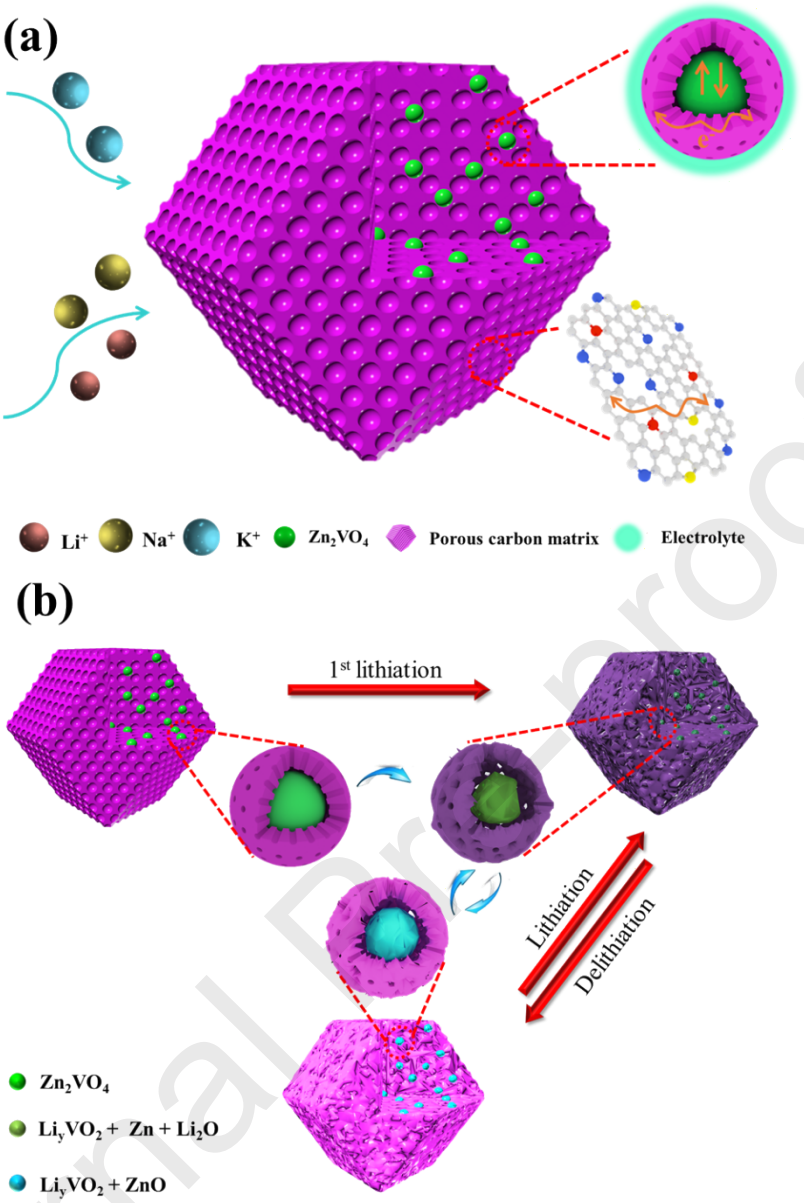

Scheme 2

CRediT author statement

Yixing Fang and **Yilan Chen** have done the experiments, analyzed the results and written the manuscript.

Lingxing Zeng has come up with the idea, guided the work and corrected the manuscript.

Tao Yang has analyzed the results and corrected the manuscript.

Qinxin Xu, Yiyi Wang and **Shihan Zeng** have participated in the synthesis of materials and resources.

Qingrong Qian has guided the work and analyzed the results.

Mingdeng Wei has corrected the manuscript.

Qinghua Chen has guided the work and supplied funding acquisition.

Declaration of interests

☒ The authors declare that they have no known competing financial interests or personal relationships that could have appeared to influence the work reported in this paper.

☐The authors declare the following financial interests/personal relationships which may be considered as potential competing interests:

Graphical abstract

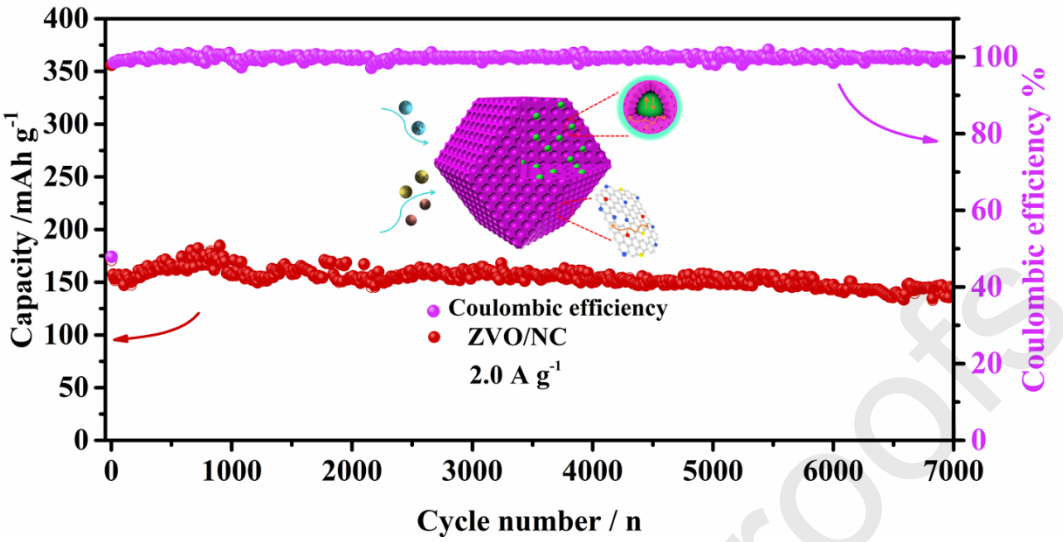

The N-doped carbon encapsulated Zn_2VO_4 polyhedron composite (ZVO/NC) with enhanced pseudocapacitive behavior for $Li^+/Na^+/K^+$ storages are designed and fabricated by a self-assembly strategy and followed by the calcination procedure.

Highlights

- The Zn_2VO_4 nanocrystals embedded in N-doped carbon was derived from V/Zn-MOFs.
- The Zn_2VO_4 phase was used as anode of SIBs/PIBs for the first time.
- Excellent stability and high capacity were realized for SIBs (145 mAh g^{-1} at 7000^{th} cycles).